Temperature-induced transformation between layered herringbone polymorphs in molecular bilayer organic semiconductors

Shunto Arai,[1,*] Satoru Inoue,[1] Mutsuo Tanaka,[2] Seiji Tsuzuki,[1] Ryusuke Kondo,[3] Reiji Kumai,[4] and Tatsuo Hasegawa[1]

[1]*Department of Applied Physics, The University of Tokyo, 7-3-1 Hongo, Bunkyo-ku, Tokyo 113-8656, Japan*
[2]*Department of Life Science & Green Chemistry, Saitama Institute of Technology, 1690 Fusaiji, Fukaya, Saitama 369-0293, Japan*
[3]*Graduate School of Natural Science and Technology, Okayama University, 1-1-1 Tsushima-naka, Kita-ku, Okayama 700-8530, Japan*
[4]*Photon Factory, Institute of Materials Structure Science, High Energy Accelerator Research Organization (KEK), 1-1 Oho, Tsukuba, Ibaraki 305-0801, Japan*

(Received 7 November 2022; accepted 1 February 2023; published 23 February 2023)

Herein we investigated the temperature-induced transformation between distinct layered herringbone (LHB) polymorphs in model organic semiconductors (OSCs) of a series of 2-mono-alkylated-benzothieno[3, 2-*b*][1]benzothiophenes (*mono*-C_n-BTBTs). The component molecules are composed of a one-sided linkage between the BTBT core and alkyl chains of various lengths. We propose that the polymorphism originates from a unique feature of LHB structures in which two types of *T*-shaped contacts are possible for BTBT cores that exhibit relatively low symmetry. Based on polarized UV-visible absorption spectra and powder x-ray diffraction analyses, we show that four long-alkylated *mono*-C_n-BTBTs ($n = 8$, 9, 10, and 11) undergo mostly irreversible structural phase transformations into short-chain-type polymorphs at elevated temperatures of approximately 85−100 °C. These transformations allowed the investigation of the stability of each polymorph in terms of thermal analysis. Based on the chain-length dependent transition entropies, we demonstrate that the polymorphic transformations are triggered by the partial entropy gain of alkyl chains, followed by the total entropy gain at solid–liquid transitions observed at higher temperatures of approximately 110 °C. We also analyzed the structure and intermolecular interactions of the four compounds. The results confirm that each molecular packing consists of a balance between the core–core and chain–chain interactions and also that the unique odd–even parity alkyl-chain-length effect of the transitions emerges as a result of the variation in interlayer stacking arrangements. We highlight the critical role of alkyl chains in terms of their large structural degrees of freedom in solution-processable and highly layered crystalline OSCs. These findings lead to a better understanding of molecular packing toward a more rational design of OSCs for efficient carrier transport.

DOI: 10.1103/PhysRevMaterials.7.025602

I. INTRODUCTION

Solution-processable organic semiconductors (OSCs) are novel materials composed of extended π-electron frameworks (π cores) linked by flexible substituents such as alkyl chains [1–5]. Some small-molecule OSCs exhibit a tendency to self-organize into a layered structure (i.e., layered crystallinity [6]), which is an essential requirement for manufacturing high-performance organic thin-film transistors (OTFTs) [7]. Alkylated OSCs based on [1]benzothieno[3, 2-*b*][1]benzothiophene (BTBT) [8–12], dinaphtho[2, 3-*b* : 2′, 3′-*f*]thieno[3, 2-*b*]thiophene (DNTT) [13–15], benzothieno[6, 5-*b*]benzothieno[3, 2-*b*]thiophenes (BTBTT) [16,17], or dinaphtho[2, 3-*d* : 2′, 3′-*d*′]benzo[1, 2-*b* : 4, 5-*b*′]dithiophene (DNBDT) [18], provide high-performance OTFTs with mobilities higher than $10\,\mathrm{cm^2\,V^{-1}\,s^{-1}}$, owing to their highly layered crystalline characteristics. These compounds should allow low-cost production of large-area and flexible electronic products under ambient conditions through print production (or "printed electronics") technologies [3,19,20].

In most high-performance OSCs, component rodlike π cores form layered herringbone (LHB)-type molecular packing, which enables efficient two-dimensional (2D) carrier transport within the layer [7,21–23]. It was recently demonstrated for several unsymmetrically alkylated BTBT- and BTNT-based OSCs that the substituted alkyl chains not only increase the solvent solubility but also enhance the layered crystallinity of the compounds [24–35], as was first demonstrated in phenyl/alkyl-substituted BTBT (Ph-BTBT-C_n) [24]. The asymmetric OSC molecules composed of rodlike π cores linked with alkyl chains provide bilayer-type herringbone (*b*-LHB) packing, where the molecules separately form a π-core layer and an inert alkyl chain layer. Pairs of the resultant unipolarly oriented molecular layers are coupled to form alternating antiparallel alignment such that the alkyl chain layers (π-core layers) are in tail-to-tail (head-to-head) contact. It was discussed that the separated formation of a

*ARAI.Shunto@nims.go.jp; National Institute for Materials Science, 1-1 Namiki, Tsukuba, Ibaraki 305-0044, Japan.

2D semiconductive π-core layer and inert alkyl-chain layers should eventually contribute to the enhancement of the layered crystallinity [26]. Another intriguing aspect is that these materials frequently undergo smectic liquid-crystal (LC) phase transitions at elevated temperatures, as observed in Ph-BTBT-C_n [10,34–36].

Among the variety of asymmetric rodlike OSCs, a series of *mono*-C_n-BTBTs is the simplest representative example [27,28,37,38] [see Fig. 1(a)]. Interestingly, the compounds did not show LC phases at elevated temperatures but formed distinctive *b*-LHB-type polymorphs, depending on the alkyl chain length; they can be classified into short-chain-type (SCP; $4 \leqslant n \leqslant 7$) and long-chain-type polymorphs (LCP; $8 \leqslant n$) [27,28]. The polymorphs likely appear as a result of the balance between the intermolecular core–core and chain–chain interactions. However, a complete understanding of the origin and variation of polymorphic phases has not yet been obtained, even though it can provide a unique opportunity to understand and control the molecular packing motif of highly layered crystalline OSCs [39–54].

In this study, we report that some *mono*-C_n-BTBTs exhibit temperature-induced transformations between distinctive polymorphic phases. We show that these observations provide a unique opportunity to investigate the stability and relationship between the polymorphic phases. We first discuss that the polymorphism observed in *mono*-C_n-BTBTs originates from a unique feature of LHB, in which two types of *T*-shaped contacts are possible between the BTBT cores. Subsequently, we show that four long-alkylated *mono*-C_n-BTBTs ($n = 8$, 9, 10, and 11) exhibit temperature-induced transformation, as shown by both polarized optical spectra and powder x-ray diffraction (p-XRD), in which Patterson analysis is useful for distinguishing the polymorphic phases. We then present the chain-length-dependent thermal analysis of the polymorphic transformations and the analysis of intermolecular interactions based on the results of complete crystal structure analyses. Based on these results, we discuss the molecular mechanism of the polymorphic transformation in *mono*-C_n-BTBTs.

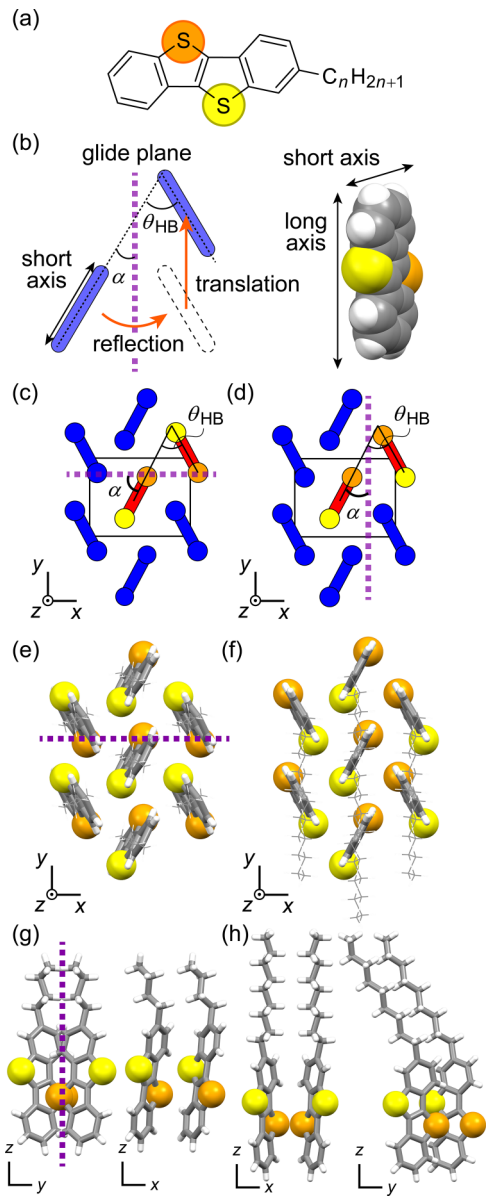

FIG. 1. (a) Chemical structure of *mono*-C_n-BTBT. (b) Schematic illustration of the *T*-shaped molecular contact, with the long axis of π-core planes aligned perpendicular to the layer, as shown in the right panel. The *T*-shape contacts are characterized by glide reflection symmetry. (c), (d) Schematic representations of distinct glide symmetries in LHB polymorphs. The glide planes are perpendicular to the (c) *y* axis and (d) *x* axis, as indicated by the purple dotted lines. (e)–(h) Molecular packing structures of *mono*-C_n-BTBTs. The packing motifs are depicted based on the crystal structures of (e), (g) $n = 4$ and (f), (h) $n = 9$. The yellow and orange colors distinguish between sulfur atoms in the BTBT core close to and far from the alkyl chain, respectively.

II. RESULTS AND DISCUSSION

A. On the distinct glide symmetries in LHB polymorphs

The LHB packing is composed of a periodic arrangement of intermolecular *T*-shaped contacts, with the long axis of the π-core planes aligned perpendicular to the layer, as shown in Figure 1(b). The π cores at the *T*-shaped contacts are typically arranged in glide reflection symmetry, where the dihedral angle (denoted as θ_{HB}) between the π-core planes is used for structural classification [55]. However, even with a common dihedral angle, two types of *T*-shaped contacts are possible when the π core involves relatively low symmetry. The two distinct LHB packings are illustrated in Figs. 1(c) and 1(d), where both packing motifs are depicted with the slipped parallel contact parallel to the vertical axis (*y* axis). The orientation of the π-core planes relative to the glide reflection plane [shown by the angle α in Figs. 1(c) and 1(d)] shows an obvious difference. The distinct nature of the packing is ascribed to the absence of reflection symmetry of the π core with regard to the short axis within the π-core plane.

This LHB polymorphism was observed in a series of *mono*-C_n-BTBTs. The molecular structure is shown in Fig. 1(a). Figures 1(e)–1(h) show the molecular packing structures of *mono*-C_4-BTBT and *mono*-C_9-BTBT. The π-core planes exhibit similar dihedral angles at the *T*-shaped

contacts, calculated as 58.0° for *mono*-C_4-BTBT and 57.0° for *mono*-C_9-BTBT. However, the difference in the *T*-shaped core–core arrangement is noticeable, and the relative positions of the sulfur atoms at the *T*-shaped contacts are distinct. Glide reflection symmetry exists in the *mono*-C_4-BTBT crystal (space group $P2_1/a$) but not in the whole *mono*-C_9-BTBT crystal (space group $P\bar{1}$). Nonetheless, the molecular arrangements within the single molecular layer of *mono*-C_9-BTBT can be understood in terms of glide reflection symmetry, as shown in Figs. 1(f) and 1(h).

To understand the effects of the polymorphism, we compared the charge transfer characteristics of *mono*-C_4-BTBT and *mono*-C_9-BTBT. Single-crystalline thin films were produced using the blade-coating technique and utilized as the active layers of OTFTs (see Supplemental Material [56] for details). Figure S1 presents the typical transfer characteristics in the saturation regime. The device mobility of the *mono*-C_4-BTBT OTFT was $\mu_{sat} = 0.20\,cm^2\,V^{-1}\,s^{-1}$ (along the *x* direction) and $0.45\,cm^2\,V^{-1}\,s^{-1}$ (along the *y* direction). These values are approximately ten times smaller than those of *mono*-C_9-BTBT OTFT, $\mu_{sat} = 2.6\,cm^2\,V^{-1}\,s^{-1}$ and $5.5\,cm^2\,V^{-1}\,s^{-1}$ along the *x* and *y* direction, respectively. These results are consistent with the calculated transfer integrals based on the crystal structures of *mono*-C_9-BTBT and *mono*-C_4-BTBT [27]; the transfer integral at the *T*-shaped contacts is much larger in the former than in the latter. These results clearly demonstrate the importance of the LHB polymorphism for the design and development of OSCs because the π cores in many OSCs exhibit relatively low molecular symmetry.

B. Polarized optical microscopy/spectroscopy for temperature-induced transformation

Figure 2(a) shows a crossed-Nicol polarized optical microscopy (POM) image of a blade-coated *mono*-C_{10}-BTBT film (see Supplemental Material [56] for details). The film was composed of several large monocrystalline domains. We extracted the largest single-crystal domain for the heating experiment, as shown in the top panel of Fig. 2(b). When we kept the sample at 100 °C, we observed a phase transformation to another solid phase composed of several monocrystalline domains with different crystalline orientations, as shown in the bottom panel of Figs. 2(b) and S2. The appearance of the films was maintained after cooling to ambient temperature.

We measured the angle-dependent polarized absorption spectra in the UV-visible range to investigate the origin of this transformation. Figure 2(c) shows the absorption spectra of the *mono*-C_{10}-BTBT single-crystalline domain before and after heating. The latter spectra were obtained by selecting a relatively large monodomain in the film for the measurement. A clear difference was observed before and after the heating treatment in the polarized absorption spectra in both the peak energy and anisotropy. This indicates a significant change in the intralayer molecular arrangements, resulting in the altered polarized excitonic absorption spectra through intermolecular interactions between exciton transition moments. Interestingly, the spectra after the heat treatment are similar to those of *mono*-C_n-BTBTs ($n = 4, 6, 7$), which are classified as SCP [28]. We also observed a similar change in

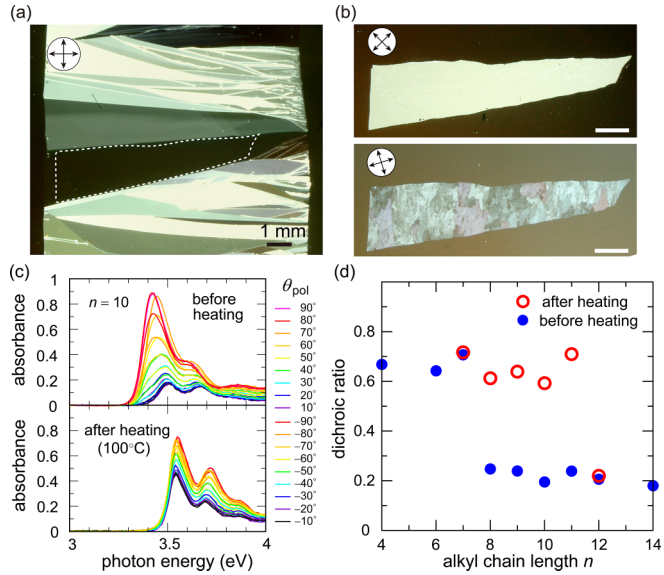

FIG. 2. (a), (b) Crossed-Nicols polarized micrographs of a blade-coated *mono*-C_{10}-BTBT film. (a) As-coated film. (b) (top) A single crystalline domain shown by the white dotted line in (a). (bottom) The same film showing polymorphic transformation with the temperature held at 100 °C. Scale bars are 1 mm. (c) Polarized optical absorption spectra of the *mono*-C_{10}-BTBT film. The absorption spectra of as-coated (top) and heated (bottom) monocrystalline domains were measured at ambient conditions. The angle $\theta_{pol} = 0°$ corresponds to the *x* axis in the LHB packing. (d) Chain length (*n*) dependence of the optical absorption anisotropy. Blue dots and unfilled red circles show the results of the as-coated and the heated single crystals, respectively. Four *mono*-C_n-BTBTs ($n = 8$–11) exhibit polymorphic transformations from LCP to SCP.

the polarized absorption spectra after the heating treatments for other *mono*-C_n-BTBTs ($n = 8$, 9, and 11) classified as LCP, as presented in Fig. S3. We found that the polarized angle-dependent absorption spectra of some crystalline domains return to those of the initial phase when measured days after the heating treatment. This indicates that the original form (i.e., LCP) is more stable for *mono*-C_{10}-BTBT under ambient conditions.

We previously demonstrated that the optical anisotropy, or dichroic ratio, crucially depends on the molecular packing motif of *mono*-C_n-BTBT, which can be utilized to discriminate between SCP (*mono*-C_4-BTBT) and LCP (*mono*-C_9-BTBT) [28]. The dichroic ratios of *mono*-C_n-BTBTs are shown in Fig. 2(d). It is evident that the packing motif of the π cores in *mono*-C_n-BTBTs ($n = 8-11$) is transformed from LCP to SCP. In contrast, we did not observe any changes in the optical anisotropies for $n = 7$ and 12 after heating.

C. Patterson map analysis of p-XRD for polymorphic transformation

Powder x-ray diffraction (p-XRD) measurements were performed to investigate the crystal structure after polymorphic transformation. Figures 3(a) and 3(b) show the typical p-XRD spectra for *mono*-C_9-BTBT in the range of $q = 1.0$–$2.4\,Å^{-1}$,

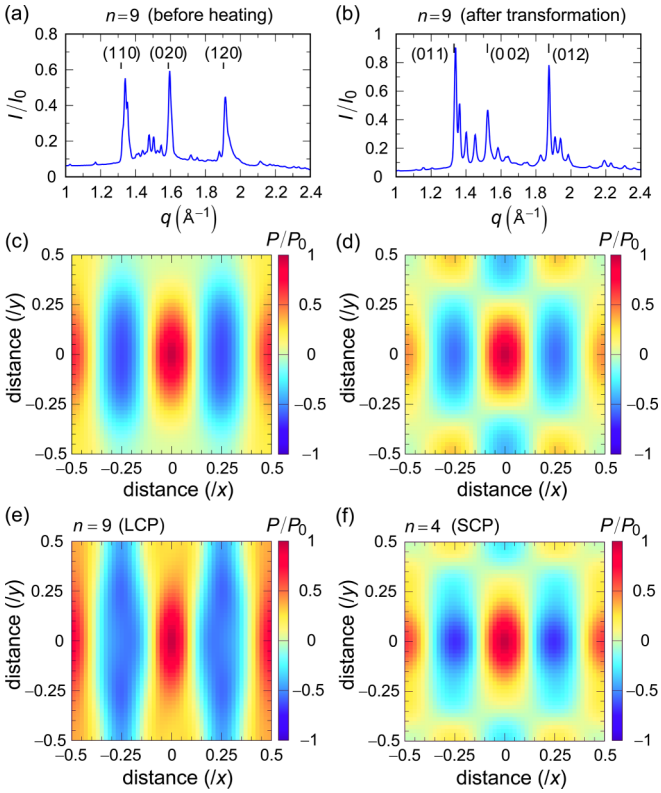

FIG. 3. Powder x-ray diffraction (p-XRD) analyses of *mono*-C_n-BTBTs. (a), (b) Diffraction patterns of the (a) recrystallized and (b) heated samples of $n = 9$. The principal peaks associated with the in-plane diffraction were indexed as (h k l). The incident x-ray photon energy was 10.0 keV. (c)–(f) Patterson maps were calculated using the in-plane diffraction intensity. The maps of (c) and (d) were calculated from the p-XRD patterns of (a) and (b), respectively. Patterson functions were also calculated using the crystal structures of (e) *mono*-C_9-BTBT (LCP) and (f) *mono*-C_4-BTBT (SCP). The x and y axes in the maps are normalized by the lattice constant of the unit cell in each crystallographic direction. The calculated intensity, P, was also normalized by the maximum intensity at the origin of coordinates, P_0.

where the intralayer diffractions are observed. Table I lists the lattice constants obtained by indexing the distinctive in-plane diffraction peaks. We also determined the lattice constants of heat-treated *mono*-C_9-BTBT through refinement using Le Bail analysis of the thin-film XRD data [57]. The lattice constants of the sample after the heating treatment became shorter in the x direction and longer in the y direction than before the heating treatment. In contrast, the lattice volume remained almost unchanged. The spectrum of the heated sample of $n = 9$ is similar to that of $n = 7$ (SCP), and similar changes are commonly observed for the series of *mono*-C_n-BTBT ($n = 8$, 9, and 10), showing polymorphic transformation (see Fig. S4). The results provide clear evidence of the phase transformation from LCP to SCP.

We analyzed the p-XRD results by using the Patterson method. The Patterson function represents the convolution of electron density with itself (see Supplemental Material [56] for details). We adopted this method to visually present the difference in the intralayer molecular packing of LHB polymorphs. Figures 3(c) and 3(d) show the calculated Patterson maps for the obtained p-XRD data. The observed features in the Patterson map present qualitative changes due to the heating treatment, which is ascribable to the variation of the electron density distribution within the two-dimensional layer. In particular, the positive value of the map was more elongated along the y axis before than after the heating treatment. This change is evident from the signal at $(0, \pm 1/2)$. A similar feature was also observed in the Patterson map of the heated *mono*-C_8-BTBT sample shown in Fig. S5. As the reference, we also calculated the Patterson functions based on the results of the full crystal structure analysis of *mono*-C_9-BTBT and *mono*-C_4-BTBT, as shown in Figs. 3(e) and 3(f). The distinct features which originate from the change of the LHB packing are more clearly observed in the comparison of the Patterson maps. The Patterson map is useful for discriminating the LHB polymorphs when only p-XRD data can be obtained owing to difficulties in full crystal structure analysis.

D. Phase diagram and transition entropy

We conducted thermal analyses of the polymorphic transformations of the recrystallized products of *mono*-C_n-BTBT using differential scanning calorimetry (DSC). Figure 4(a) shows typical DSC curves for the series of *mono*-C_n-BTBTs ($n = 8 - 11$). The DSC curves for all the samples exhibit small endothermic peaks at approximately 85–100 °C owing to polymorphic transformations, which are followed by sharp endothermic peaks associated with the melting transitions at around 110 °C. The onset temperatures of the endothermic peaks for the polymorphic transitions are roughly independent of the heating rate, whereas the peak height and peak

TABLE I. The intralayer lattice constants of *mono*-C_n-BTBTs along x and y crystallographic directions.

n	$//x$ (Å)	$//y$ (Å)	Lattice volume (Å^3)	Cryst. type	Method[a]	Ref.
4	5.8764	8.1910	1543.9	SCP	SC-XRD	[27]
8 (heated)	5.7560	8.2873	1935.0	SCP	p-XRD	[38]
8 (as-grown)	5.9616	7.8701	1901.7	LCP	SC-XRD	This work
9 (heated)	5.755	8.256	2058.5	SCP	thin-film XRD and p-XRD	This work
9 (as-grown)	5.97616	7.9219	2043.3	LCP	SC-XRD	[27]
10	5.96528	7.8482	2107.1	LCP	SC-XRD	This work
11	5.95355	7.84939	2220.6	LCP	SC-XRD	This work

[a]SC-XRD: Single crystal x-ray diffraction.

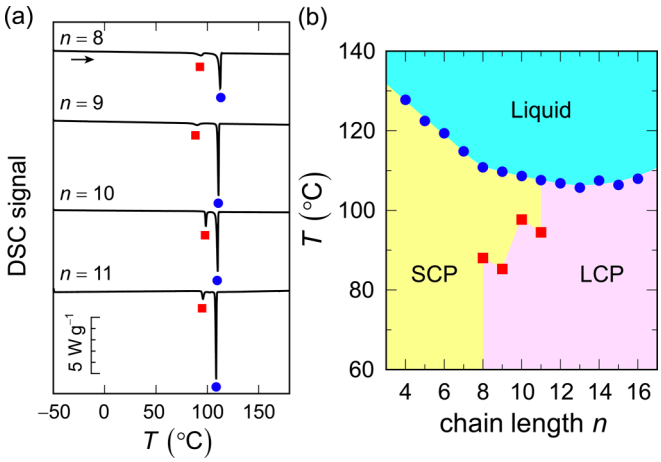

FIG. 4. (a) Typical DSC curves of *mono*-C_n-BTBTs ($n = 8$, 9, 10, and 11) during the heating process. A sharp endothermic peak at around 110 °C in each curve corresponds to the melting point. The broad peak before reaching the melting point corresponds to the polymorphic phase transition. (b) The chain-length–temperature phase diagram for the *mono*-C_n-BTBT ($n = 4$–16). The filled blue circles and red squares indicate the melting and the polymorphic transition points, respectively.

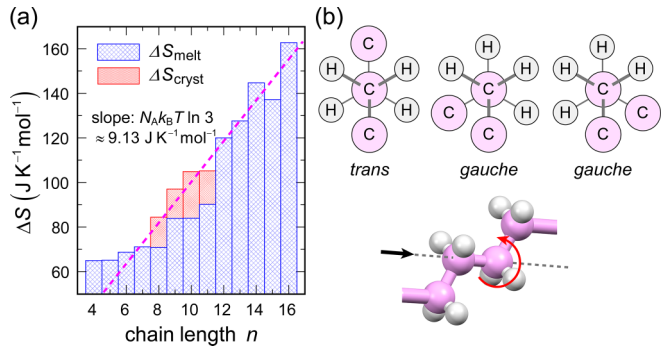

FIG. 5. (a) Chain-length (n) dependence of entropy change at the melting point (ΔS_{melt}) and the polymorphic transition ($\Delta S_{\mathrm{cryst}}$). The dashed line represents the slope of $N_A k_B \cdot \ln 3 \approx 9.13\,\mathrm{J\,K^{-1}}$ (mol of $-CH_2-$)$^{-1}$. (b) Schematics for the three conformations of neighboring methylene groups. The top figure shows the conformation of methylene groups observed from the direction along the chemical bond, as indicated by the black arrow in the bottom figure.

temperature depend sensitively on the heating rate, as shown in Fig. S6(a). The heating rate dependence of peak temperature indicates the gradual nature of the polymorphic transformations. Additionally, a clear exothermic peak due to polymorphic transformation back to the initial phase was not observed in the cooling run, as shown in Fig. S6(b). This led to the absence of small endothermic peaks at approximately 85–100 °C in the second heating run, as shown in Fig. S6(c). These features are consistent with the POM observations. Note that the exothermic peak due to solidification from the liquid phase also depends considerably on the cooling rate, as shown in Fig. S6(b). The observed features indicate that crystallization in *mono*-C_n-BTBTs proceeds very slowly in the supercooled state.

The phase transition temperatures were extracted from the onset of the endothermic peaks in the first heating run of the DSC curves. Figure 4(b) shows the chain-length–temperature phase diagram for *mono*-C_n-BTBT ($n = 4$–16). Polymorphic phase transformation is observed at the intermediate chain length ($n = 8$–11) because of the competition between the SCP and LCP. The transition temperature tends to increase with chain length, but it also depends on the parity of the number of carbon atoms in the alkyl chains, which will be discussed in Sec. II F.

We analyzed the DSC curves during the first heating run to evaluate the transition entropy from the crystalline state at ambient conditions to the liquid state at high temperatures. Figure 5(a) shows the transition entropy plotted as a function of chain length (number of carbon atoms in the substituted alkyl chains). The transition entropy for the melting transition increased considerably with increasing alkyl chain length. In the figure, we also show the slope of $N_A k_B$ ln 3 ($\approx$9.13 J/mol K), where N_A and k_B are Avogadro's number and the Boltzmann constant, respectively. We found that the transition entropy for *mono*-C_n-BTBTs at $n \geqslant 12$ increases almost linearly with chain length, with the slope roughly proportional to $N_A k_B$ ln 3. A similar alkyl-chain-length dependence of transition entropy has been reported for the melting transition of other liquid crystalline compounds [58–60]. The factor 3 is ascribable to the conformational degrees of freedom of the alkyl chains, as shown in Fig. 5(b). The alkyl chains are linearly extended (i.e., all-trans) in the crystal phase; however, when the compounds are melted, each methylene group can take three available conformations involving one trans- and two gauche- conformations. The observed results indicate that the alkyl chains with large conformational degrees of freedom work as an entropy reservoir and thus play fundamental roles in the melting transition of *mono*-C_n-BTBTs.

In contrast, the slope of the entropy change in the melting transition for *mono*-C_n-BTBTs at $n = 8$–11 is approximately 1/2–1/3 times smaller than that of $N_A k_B$ ln 3. Interestingly, the total transition entropy for both polymorphic and melting transitions is linearly dependent on the chain length, whose increasing rate is close to that of $N_A k_B$ ln 3, and thus, the slope is continuously connected with the compounds at $n \geqslant 12$, as seen in Fig. 5(a). This suggests that the LCP with $n = 8$–11 undergoes a structural transformation to the SCP to achieve a partial entropy gain before complete melting. We propose that the alkyl chain ordering should fluctuate more in the SCP than in the LCP. This feature is observed by the thermal ellipsoids at room temperature (see Fig. S7), even though the chain order was confirmed by crystal structure analysis. This partial melting of the alkyl chain leads to the rearrangement of the π cores to the SCP.

E. Crystal structures and intermolecular interaction analysis

In this study, we successfully conducted additional full crystal structure analyses for *mono*-C_n-BTBT single crystals of $n = 8$, 10, and 11 at ambient conditions (see Supplemental Material [56] and Fig. S8). The obtained structures are isomorphous with those of *mono*-C_9-BTBT, which confirms the validity of the analysis using optical absorption and p-XRD measurements [28]. Using the crystal structure data and that of *mono*-C_4-BTBT and heated *mono*-C_8-BTBT [38], we

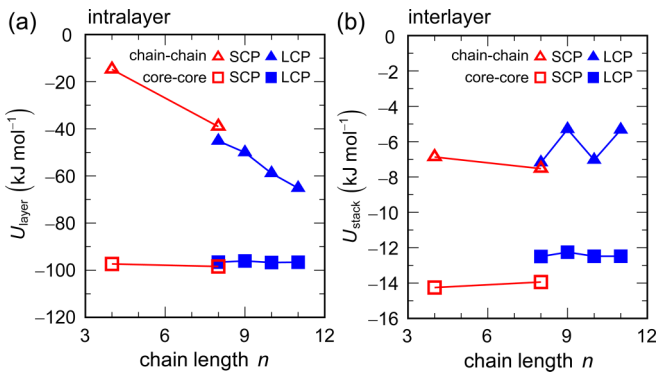

FIG. 6. (a), (b) Chain-length dependence of the sum of the (a) intralayer and (b) interlayer interaction energies. The core–core (square symbols) and chain–chain (triangle symbols) interactions in the *mono*-C_n-BTBT crystals were calculated using the structures of the fragments in the crystals. The red-open and blue-filled symbols indicate the results calculated using the crystal structures of SCP and LCP, respectively.

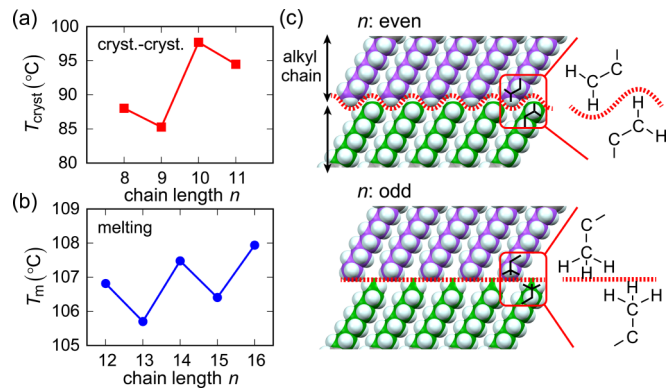

FIG. 7. (a), (b) Chain length (n) dependence of the phase transition temperatures of *mono*-C_n-BTBTs from the LCP. (a) Crystal–crystal transition temperatures at $8 \leqslant n \leqslant 11$. (b) Melting temperatures at $12 \leqslant n \leqslant 16$. In both cases, the phase transition temperature of $n = 2m$ ($m \geqslant 4$) is higher than that of $n = 2m + 1$ despite the increase in the chain length. (c) Interlayer stacking structures of alkyl side chains represented by a space-filling model. Even (top) and odd (bottom) number of carbon atoms in the alkyl chain. The stacking motifs are depicted based on the crystal structures of the LCP of $n = 8$ and 9. The atomic arrangements surrounded by the red frames are schematically illustrated in the right panels.

evaluated the lattice energy (U_{lattice}) using dispersion-corrected density functional theory (DFT) calculations under periodic boundary conditions (see Supplemental Material [56] and Refs. [61–65] for details). The results are shown in Fig. S9(a). We found that the U_{lattice} increased almost linearly as the alkyl chain length increased.

To investigate the origin of the change in U_{lattice}, we decomposed the intermolecular interactions into four different types: Intralayer/interlayer core–core interactions and intralayer/interlayer chain–chain interactions; the calculated results are plotted in Fig. 6 (see Supplemental Material [56] and Refs. [64–68] for details). The sum of the decomposed interaction energies is approximately coincident with the lattice energy, as shown in Fig. S9(b). We found that the intralayer interactions are almost 10 times larger than the interlayer interactions, and that the intralayer chain–chain interaction primarily increases with increasing chain length. Notably, the change from the LCP to the SCP causes a slight increase (1.85 kJ/mol) of the intralayer core–core interaction but a decrease (6.08 kJ/mol) of the intralayer chain–chain interaction, as seen in Fig. 6(a). These results demonstrate that the intralayer chain–chain interaction is more significant in determining the intermolecular arrangements of the LCP than that of the SCP. The intralayer interaction analyses also suggest that the SCP is slightly more stable in terms of the π-core arrangements, as evidenced by the crystal structure of BTBT without alkyl chain substitution [27], which shows an SCP crystal structure. We conclude that the polymorphic transformation is triggered by a decrease in the effective intralayer chain–chain interactions in the LCP due to increasing temperature, eventually resulting in the transition to an SCP owing to the stability of the π-core arrangement.

F. The observed odd–even chain length effect

The odd–even alkyl-chain-length effect is a unique characteristic of organic compounds that involve alkyl chains. This effect originates from the fact that the direction of the terminal C–C bond depends on the parity of the number of carbon atoms [5,69,70]. We found that the *mono*-C_n-BTBTs present an odd–even chain length effect on the phase transition temperature for both polymorphic transformations at $n = 8$–11 and melting transitions at $n \geqslant 12$, as shown in Figs. 7(a) and 7(b), respectively. Notably, both effects were clearly observed in the transitions from LCP. In fact, the interlayer chain–chain interaction clearly depends on the odd–even number of carbon atoms in the alkyl chains, where the difference is as large as ~2 kJ/mol, as shown in Fig. 6(b).

Figure 7(c) shows the molecular arrangements around the contacts between the alkyl chain layers for both even and odd chain lengths. In the case of an even number (*mono*-C_8-BTBT), the terminal C–C bond is largely inclined from the layer normal, so that one of the end hydrogen atoms can penetrate the counter alkyl-chain layer, causing relatively strong interlayer interactions. In contrast, in the case of an odd number (*mono*-C_9-BTBT), the terminal C–C bond is almost parallel to the layer normal, so that the three hydrogen atoms are equally arranged on the layer surface and do not penetrate the counter alkyl-chain layer. Such a clear dependence of the interlayer interactions on the odd–even number explains the observed odd–even chain effect of the phase transition temperature in *mono*-C_n-BTBTs. Notably, a similar dependence on the packing geometry was observed in other BTBT derivatives, such as Ph-BTBT-C_n and *di*-C_n-BTBTs (see Fig. S10).

III. CONCLUSION

We demonstrated unique temperature-induced polymorphic transformations between distinct LHB polymorphs in model layered-crystalline OSCs of *mono*-C_n-BTBTs. Four types of LCP at $n = 8$–11 present mostly irreversible

structural phase transformation into the SCP at elevated temperatures of approximately 85–100 °C, as confirmed by POM observation, polarized optical spectroscopy, p-XRD, and thermal analysis. The transformations are ascribable to the appearance of two unique types of LHB packing derived from the lower symmetry of the BTBT π cores. Based on the thermal analyses, we found that the polymorphic transformations were triggered by the partial entropy gain of the alkyl chains, followed by the total entropy gain at the melting transitions observed at higher temperatures. Intermolecular interaction analyses based on full crystal structure data allowed us to clarify that the intralayer core–core interaction plays a principal role in the SCP, whereas the intralayer chain–chain interaction plays a more significant role in the LCP. Additionally, a unique odd–even chain-length effect was observed as the transition temperatures for polymorphic/melting transitions from the LCP varied owing to the variation in interlayer chain–chain interactions.

Our results demonstrate the significant influence of alkyl chains with large structural degrees of freedom on the properties of highly layered crystalline OSCs, which are the most promising materials for producing high-performance OTFTs. Understanding the stability and competition between the structural phases is crucial for the optimal design and development of OSC molecules, and thin-film processing toward the goal of high-performance and printed electronics applications.

ACKNOWLEDGMENTS

The authors are grateful to Nippon Kayaku Co., Ltd. for providing BTBT, R. Nakamura for his help with thin-film formation and characterization, and T. Utsumi for his support with the synthesis of *mono*-C_n-BTBT compounds. This study was partly supported by JSPS KAKENHI Grants No. JP19H02579, No. JP19H05321, No. JP20H05867, No. JP21K05209, No. JP21H05234, and No. JP22H01933, and JST CREST Grant No. JPMJCR18J2. S.A. also thanks the Murata Science Foundation and Kao Foundation for Arts and Sciences. The synchrotron x-ray experiments were performed with the approval of the Photon Factory Program Advisory Committee (Grants No. 2017S2-001 and No. 2020S2-001).

[1] J. Mei, Y. Diao, A. L. Appleton, L. Fang, and Z. Bao, Integrated materials design of organic semiconductors for field-effect transistors, J. Am. Chem. Soc. **135**, 6724 (2013).

[2] J. Mei and Z. Bao, Side chain engineering in solution-processable conjugated polymers, Chem. Mater. **26**, 604 (2014).

[3] H. Sirringhaus, 25th anniversary article: Organic field-effect transistors: The path beyond amorphous silicon, Adv. Mater. **26**, 1319 (2014).

[4] B. Kang, F. Ge, L. Qiu, and K. Cho, Effective use of electrically insulating units in organic semiconductor thin films for high-performance organic transistors, Adv. Electron. Mater. **3**, 1600240 (2017).

[5] T. Lei, J.-Y. Wang, and J. Pei, Roles of flexible chains in organic semiconducting materials, Chem. Mater. **26**, 594 (2014).

[6] H. Minemawari, J. Tsutsumi, S. Inoue, T. Yamada, R. Kumai, and T. Hasegawa, Crystal structure of asymmetric organic semiconductor 7-decyl-2-phenyl[1]benzothieno[3, 2-*b*][1]benzothiophene, Appl. Phys. Express **7**, 091601 (2014).

[7] S. K. Park, J. H. Kim, and S. Y. Park, Organic 2D optoelectronic crystals: Charge transport, emerging functions, and their design perspective, Adv. Mater. **30**, 1704759 (2018).

[8] H. Ebata, T. Izawa, E. Miyazaki, K. Takimiya, M. Ikeda, H. Kuwabara, and T. Yui, Highly soluble [1]benzothieno [3, 2-*b*] benzothiophene (BTBT) derivatives for high-performance, solution-processed organic field-effect transistors, J. Am. Chem. Soc. **129**, 15732 (2007).

[9] H. Minemawari, T. Yamada, H. Matsui, J. Tsutsumi, S. Haas, R. Chiba, R. Kumai, and T. Hasegawa, Inkjet printing of single-crystal films, Nature (London) **475**, 364 (2011).

[10] H. Iino, T. Usui, and J.-I. Hanna, Liquid crystals for organic thin-film transistors, Nat. Commun. **6**, 6828 (2015).

[11] T. Hamai, S. Arai, H. Minemawari, S. Inoue, R. Kumai, and T. Hasegawa, Tunneling and origin of large access resistance in layered-crystal organic transistors, Phys. Rev. Appl **8**, 054011 (2017).

[12] K. He, W. Li, H. Tian, J. Zhang, D. Yan, Y. Geng, and F. Wang, Asymmetric conjugated molecules based on [1]benzothieno [3, 2-*b*][1]benzothiophene for high-mobility organic thin-film transistors: Influence of alkyl chain length, ACS Appl. Mater. Interfaces **9**, 35427 (2017).

[13] M. J. Kang, I. Doi, H. Mori, E. Miyazaki, K. Takimiya, M. Ikeda, and H. Kuwabara, Alkylated dinaphtho[2, 3-*b* : 2′, 3′-*f*] thieno[3, 2-*b*]thiophenes (C_n-DNTTs): Organic semiconductors for high-performance thin-film transistors, Adv. Mater. **23**, 1222 (2011).

[14] B. Peng, Z. Wang, and P. K. L. Chan, A simulation-assisted solution-processing method for a large-area, high-performance C_{10}-DNTT organic semiconductor crystal, J. Mater. Chem. C **4**, 8628 (2016).

[15] B. Peng, S. Huang, Z. Zhou, and P. K. L. Chan, Solution-processed monolayer organic crystals for high-performance field-effect transistors and ultrasensitive gas sensors, Adv. Funct. Mater. **27**, 1700999 (2017).

[16] K. He, S. Zhou, W. Li, H. Tian, Q. Tang, J. Zhang, D. Yan, Y. Geng, and F. Wang, Five-ring-fused asymmetric thienoacenes for high mobility organic thin-film transistors: The influence of the position of the S atom in the terminal thiophene ring, J. Mater. Chem. C **7**, 3656 (2019).

[17] T. Higashino, S. Inoue, S. Arai, H. Matsui, N. Toda, S. Horiuchi, R. Azumi, and T. Hasegawa, Architecting layered crystalline organic semiconductors based on unsymmetric π-extended thienoacenes, Chem. Mater. **33**, 7379 (2021).

[18] C. Mitsui, T. Okamoto, M. Yamagishi, J. Tsurumi, K. Yoshimoto, K. Nakahara, J. Soeda, Y. Hirose, H. Sato, A. Yamano, T. Uemura, and J. Takeya, High-performance solution-processable N-shaped organic semiconducting materials with stabilized crystal phase, Adv. Mater. **26**, 4546 (2014).

[19] M. Berggren, D. Nilsson, and N. D. Robinson, Organic materials for printed electronics, Nat. Mater. **6**, 3 (2007).

[20] S. Duan, T. Wang, B. Geng, X. Gao, C. Li, J. Zhang, Y. Xi, X. Zhang, X. Ren, and W. Hu, Solution-processed centimeter-scale highly aligned organic crystalline arrays for high-performance organic field-effect transistors, Adv. Mater. **32**, 1908388 (2020).

[21] H. Dong, X. Fu, J. Liu, Z. Wang, and W. Hu, 25th anniversary article: Key points for high-mobility organic field-effect transistors, Adv. Mater. **25**, 6158 (2013).

[22] K. Takimiya, I. Osaka, T. Mori, and M. Nakano, Organic semiconductors based on[1]benzothieno[3, 2-*b*][1]benzothiophene substructure, Acc. Chem. Res. **47**, 1493 (2015).

[23] X. Zhang, H. Dong, and W. Hu, Organic semiconductor single crystals for electronics and photonics, Adv. Mater. **30**, 1801048 (2018).

[24] S. Inoue, H. Minemawari, J. Tsutsumi, M. Chikamatsu, T. Yamada, S. Horiuchi, M. Tanaka, R. Kumai, M. Yoneya, and T. Hasegawa, Effects of substituted alkyl chain length on solution-processable layered organic semiconductor crystals, Chem. Mater. **27**, 3809 (2015).

[25] S. Inoue, S. Shinamura, Y. Sadamitsu, S. Arai, S. Horiuchi, M. Yoneya, K. Takimiya, and T. Hasegawa, Extended and modulated thienothiophenes for thermally durable and solution-processable organic semiconductors, Chem. Mater. **30**, 5050 (2018).

[26] T. Higashino, S. Inoue, Y. Sadamitsu, S. Arai, S. Horiuchi, and T. Hasegawa, Bilayer-type layered herringbone packing in 3-*n*-octyl-9-phenyl-benzothieno[3,2-*b*]naphtho[2,3-*b*]thiophene, Chem. Lett. **48**, 453 (2019).

[27] H. Minemawari, M. Tanaka, S. Tsuzuki, S. Inoue, T. Yamada, R. Kumai, Y. Shimoi, and T. Hasegawa, Enhanced layered-herringbone packing due to long alkyl chain substitution in solution-processable organic semiconductors, Chem. Mater. **29**, 1245 (2017).

[28] S. Arai, K. Morita, J. Tsutsumi, S. Inoue, M. Tanaka, and T. Hasegawa, Layered-herringbone polymorphs and alkyl-chain ordering in molecular bilayer organic semiconductors, Adv. Funct. Mater. **30**, 1906406 (2020).

[29] Y. Shibata, J. Tsutsumi, S. Matsuoka, H. Minemawari, S. Arai, R. Kumai, and T. Hasegawa, Unidirectionally crystallized stable *n*-type organic thin-film transistors based on solution-processable donor–acceptor compounds, Adv. Electron. Mater. **3**, 1700097 (2017).

[30] S. Arai, S. Inoue, T. Hamai, R. Kumai, and T. Hasegawa, Semiconductive single molecular bilayers realized using geometrical frustration, Adv. Mater. **30**, 1707256 (2018).

[31] G. Kitahara, S. Inoue, T. Higashino, M. Ikawa, T. Hayashi, S. Matsuoka, S. Arai, and T. Hasegawa, Meniscus-controlled printing of single-crystal interfaces showing extremely sharp switching transistor operation, Sci. Adv. **6**, eabc8847 (2020).

[32] T. Higashino, S. Arai, S. Inoue, S. Tsuzuki, Y. Shimoi, S. Horiuchi, T. Hasegawa, and R. Azumi, Architecting layered molecular packing in substituted benzobisbenzothiophene (BBBT) semiconductor crystals, CrystEngComm **22**, 3618 (2020).

[33] Y. Ogawa, K. Yamamoto, C. Miura, S. Tamura, M. Saito, M. Mamada, D. Kumaki, S. Tokito, and H. Katagiri, Asymmetric alkylthienyl thienoacenes derived from anthra[2, 3-*b*]thieno [2, 3-*d*]thiophene for solution-processable organic semiconductors, ACS Appl. Mater. Interfaces **9**, 9902 (2017).

[34] H. Iino, T. Kobori, and J.-I. Hanna, Improved thermal stability in organic FET fabricated with a soluble BTBT derivative, J. Non-Cryst. Solids **358**, 2516 (2012).

[35] S. Guo, Y. He, I. Murtaza, J. Tan, J. Pan, Y. Guo, Y. Zhu, Y. He, and H. Meng, Alkoxy substituted [1]benzothieno [3, 2-*b*][1]benzothiophene derivative with improved performance in organic thin film transistors, Org. Electron. **56**, 68 (2018).

[36] Y. He, M. Sezen, D. Zhang, A. Li, L. Yan, H. Yu, C. He, O. Goto, Y.-L. Loo, and H. Meng, High performance OTFTs fabricated using a calamitic liquid crystalline material of 2-(4-dodecyl phenyl)[1]benzothieno[3, 2-*b*][1]benzothiophene, Adv. Electron. Mater. **2**, 1600179 (2016).

[37] A. Y. Amin, A. Khassanov, K. Reuter, T. Meyer-Friedrichsen, and M. Halik, Low-voltage organic field effect transistors with a 2-tridecyl[1]benzothieno[3, 2-*b*][1]benzothiophene semiconductor layer, J. Am. Chem. Soc. **134**, 16548 (2012).

[38] G. Gbabode, M. Dohr, C. Niebel, J.-Y. Balandier, C. Ruzié, P. Négrier, D. Mondieig, Y. H. Geerts, R. Resel, and M. Sferrazza, X-ray structural investigation of nonsymmetrically and symmetrically alkylated [1]benzothieno[3, 2-*b*]benzothiophene derivatives in bulk and thin films, ACS Appl. Mater. Interfaces **6**, 13413 (2014).

[39] L. Huang, Q. Liao, Q. Shi, H. Fu, J. Ma, and J. Yao, Rubrene micro-crystals from solution routes: Their crystallography, morphology and optical properties, J. Mater. Chem. **20**, 159 (2010).

[40] T. Matsukawa, M. Yoshimura, K. Sasai, M. Uchiyama, M. Yamagishi, Y. Tominari, Y. Takahashi, J. Takeya, Y. Kitaoka, Y. Mori, and T. Sasaki, Growth of thin rubrene single crystals from 1-propanol solvent, J. Cryst. Growth **312**, 310 (2010).

[41] C. C. Mattheus, A. B. Dros, J. Baas, G. T. Oostergetel, A. Meetsma, J. L. de Boer, and T. T. M. Palstra, Identification of polymorphs of pentacene, Synth. Met. **138**, 475 (2003).

[42] T. Siegrist, C. Besnard, S. Haas, M. Schiltz, P. Pattison, D. Chernyshov, B. Batlogg, and C. Kloc, A polymorph lost and found: The high-temperature crystal structure of pentacene, Adv. Mater. **19**, 2079 (2007).

[43] Y. Diao, K. M. Lenn, W.-Y. Lee, M. A. Blood-Forsythe, J. Xu, Y. Mao, Y. Kim, J. A. Reinspach, S. Park, A. Aspuru-Guzik, G. Xue, P. Clancy, Z. Bao, and S. C. B. Mannsfeld, Understanding polymorphism in organic semiconductor thin films through nanoconfinement, J. Am. Chem. Soc. **136**, 17046 (2014).

[44] O. D. Jurchescu, D. A. Mourey, S. Subramanian, S. R. Parkin, B. M. Vogel, J. E. Anthony, T. N. Jackson, and D. J. Gundlach, Effects of polymorphism on charge transport in organic semiconductors, Phys. Rev. B **80**, 085201 (2009).

[45] J. Chen, M. Shao, K. Xiao, A. J. Rondinone, Y.-L. Loo, P. R. C. Kent, B. G. Sumpter, D. Li, J. K. Keum, P. J. Diemer, J. E. Anthony, O. D. Jurchescu, and J. Huang, Solvent-type-dependent polymorphism and charge transport in a long fused-ring organic semiconductor, Nanoscale **6**, 449 (2014).

[46] L. Antolini, G. Horowitz, F. Kouki, and F. Garnier, Polymorphism in oligothiophenes with an even number of thiophene subunits, Adv. Mater. **10**, 382 (1998).

[47] M. Campione, S. Tavazzi, M. Moret, and W. Porzio, Crystal-to-crystal phase transition in α-quaterthiophene: An optical and structural study, J. Appl. Phys. **101**, 083512 (2007).

[48] G. Schweicher, N. Paquay, C. Amato, R. Resel, M. Koini, S. Talvy, V. Lemaur, J. Cornil, Y. Geerts, and G. Gbabode, Toward single crystal thin films of terthiophene by directional

crystallization using a thermal gradient, Cryst. Growth Des. **11**, 3663 (2011).

[49] P. He, Z. Tu, G. Zhao, Y. Zhen, H. Geng, Y. Yi, Z. Wang, H. Zhang, C. Xu, J. Liu, X. Lu, X. Fu, Q. Zhao, X. Zhang, D. Ji, L. Jiang, H. Dong, and W. Hu, Tuning the crystal polymorphs of alkyl thienoacene via solution self-assembly toward air-stable and high-performance organic field-effect transistors, Adv. Mater. **27**, 825 (2015).

[50] H. Chung, S. Chen, N. Sengar, D. W. Davies, G. Garbay, Y. H. Geerts, P. Clancy, and Y. Diao, Single atom substitution slters the polymorphic transition mechanism in qrganic electronic Crystals, Chem. Mater. **31**, 9115 (2019).

[51] B. Wedl, R. Resel, G. Leising, B. Kunert, I. Salzmann, M. Oehzelt, N. Koch, A. Vollmer, S. Duhm, O. Werzer, G. Gbabode, M. Sferrazzag, and Y. Geerts, Crystallisation kinetics in thin films of dihexyl-terthiophene: The appearance of polymorphic phases, RSC Adv. **2**, 4404 (2012).

[52] J. Chen, J. Anthony, and D. C. Martin, Thermally induced solid-state phase transition of bis (triisopropylsilylethynyl) pentacene crystals, J. Chem. Phys. B **110**, 16397 (2006).

[53] H. Chung, D. Dudenko, F. Zhang, G. D'avino, C. Ruzié, A. Richard, G. Schweicher, J. Cornil, D. Beljonne, Y. Geerts, and Y. Diao, Rotator side chains trigger cooperative transition for shape and function memory effect in organic semiconductors, Nat. Commun. **9**, 278 (2018).

[54] H. Chung, S. Chen, B. Patel, G. Garbay, Y. H. Geerts, and Y. Diao, Understanding the role of bulky side chains on polymorphism of BTBT-based organic semiconductors, Crys. Growth Des. **20**, 1646 (2020).

[55] G. R. Desiraju and A. Gavezzotti, Crystal structures of polynuclear aromatic hydrocarbons. Classification, rationalization and prediction from molecular structure, Acta Cryst. B **45**, 473 (1989).

[56] See Supplemental Material at http://link.aps.org/supplemental/10.1103/PhysRevMaterials.7.025602 for materials and methods, and Supplemental Figs. S1–S10. Crystallographic information for compounds *mono*-C_8-BTBT, *mono*-C_{10}-BTBT, *mono*-C_{11}-BTBT is available in CCDC 2240318, 2240319, 2240320, respectively.

[57] A. Le Bail, H. Duroy, and J. L. Fourquet, *ab initio* structure determination of $LiSbWO_6$ by x-ray powder diffraction, Mater. Res. Bull. **23**, 447 (1988).

[58] M. Sorai and K. Saito, Alkyl chains acting as entropy reservoir in liquid crystalline materials, Chem. Rec. **3**, 29 (2003).

[59] K. Horiuchi, Y. Yamamura, R. Pełka, M. Sumita, S. Yasuzuka, M. Massalska-Arodz, and K. Saito, Entropic contribution of flexible terminals to mesophase formation revealed by thermodynamic analysis of 4-alkyl-4′-isothiocyanatobiphenyl (*n*TCB), J. Phys. Chem. B **114**, 4870 (2010).

[60] K. Nikaido, S. Inoue, R. Kumai, T. Higashino, S. Matsuoka, S. Arai, and T. Hasegawa, Mixing-induced orientational ordering in liquid-crystalline organic semiconductors, Adv. Mater. Interf. **9**, 2201789 (2022).

[61] P. Giannozzi *et al.*, QUANTUM ESPRESSO: A modular and open-source software project for quantum simulations of materials, J. Phys.: Condens. Matter **21**, 395502 (2009).

[62] P. Giannozzi *et al.*, Advanced capabilities for materials modelling with QUANTUM ESPRESSO, J. Phys.: Condens. Matter **29**, 465901 (2017).

[63] J. P. Perdew, K. Burke, and M. Ernzerhof, Generalized Gradient Approximation Made Simple, Phys. Rev. Lett. **77**, 3865 (1996).

[64] S. Grimme, J. Antony, S. Ehrlich, and H. Krieg, A consistent and accurate *ab initio* parametrization of density functional dispersion correction (DFT-D) for the 94 elements H-Pu, J. Chem. Phys. **132**, 154104 (2010).

[65] S. Tsuzuki and T. Uchimaru, Accuracy of intermolecular interaction energies, particularly those of hetero-atom containing molecules obtained by DFT calculations with Grimme's D2, D3 and D3BJ dispersion corrections, Phys. Chem. Chem. Phys. **22**, 22508 (2020).

[66] M. J. Frisch *et al.*, *Gaussian 16* (Wallingford, Connecticut, 2016).

[67] B. J. Ransil, Studies in molecular structure. IV. Potential curve for the interaction of two helium atoms in single-configuration LCAO MO SCF approximation, J. Chem. Phys. **34**, 2109 (1961).

[68] S. F. Boys and F. Bernardi, The calculation of small molecular interactions by the differences of separate total energies. Some procedures with reduced errors, Mol. Phys. **19**, 553 (1970).

[69] A. D. Bond, On the crystal structures and melting point alternation of the *n*-alkyl carboxylic acids, New J. Chem. **28**, 104 (2004).

[70] L. P. de la Rama, L. Hu, Z. Ye, M. Y. Efremov, and L. H. Allen, Size effect and odd–even alternation in the melting of single and stacked AgSC*n* layers: Synthesis and nanocalorimetry measurements, J. Am. Chem. Soc. **135**, 14286 (2013).